RUSSIAN JOURNAL OF ELECTROCHEMISTRY, 2025, Vol. 61, No. 1, pp. 52–62

OXYGEN-ION AND PROTON TRANSPORT IN Y^{3+}-DOPED HEXAGONAL PEROVSKITE $BA_7IN_6AL_2O_{19}$[1]

© 2025 I. E. Animitsa*, R. D. Andreev, D. V. Korona, A. R. Gilev, S. S. Nokhrin

Ural Federal University named after the First President of Russia B. N. Yeltsin, Yekaterinburg, Russia

**e-mail: Irina.animitsa@urfu.ru*

Received: July 16, 2024

Revised: September 19, 2024

Accepted: September 27, 2024

Abstract. In this work, the thermal and electrical properties of the Y^{3+}-doped $Ba_7In_{5.9}Y_{0.1}Al_2O_{19}$ phase, characterized by a hexagonal perovskite structure (a = 5.935(7) Å, c = 37.736(8) Å), were studied. It has been established that the phase is capable of incorporating protons and exhibiting proton conductivity. The introduction of an isovalent dopant, yttrium, led to an increase in the concentration of protons (up to the limiting values of $Ba_7In_{5.9}Y_{0.1}Al_2O_{19}\cdot 0.55H_2O$), as a result of an increase in the unit cell volume and, accordingly, the free space for the placement of OH^- groups in an oxygen-deficient block containing coordination-unsaturated polyhedra [BaO_9]. Isovalent doping led to an increase in the oxygen-ion conductivity, which is due to an increase in interatomic distances and a decrease in the migration activation energy. In a humid atmosphere ($pH_2O = 1.92\cdot 10^{-2}$ atm), the $Ba_7In_{5.9}Y_{0.1}Al_2O_{19}$ phase exhibited higher values of proton conductivity compared to the matrix compound $Ba_7In_6Al_2O_{19}$ and below 500 °C it was characterized by dominant proton transport both in air and in a wide range of pO_2 (10^{-18}–0.21 atm).

Keywords: *hexagonal perovskite, hydration, oxygen-ion conductivity, proton conductivity, ion transport numbers*

DOI: 10.31857/S04248570250103e2

INTRODUCTION

Research on high-temperature proton conductivity in oxide systems has been ongoing for more than 40 years, starting with the first works of H. Iwahara made on ABO_3 perovskites [1–4]. The possibility of proton defects in these compounds is due to the presence of oxygen vacancies, which are determined by the introduction of an acceptor dopant. When processed in an atmosphere containing water vapor, proton defects are formed in the structure of such compounds, which causes proton conductivity:

$$V_o^{\bullet\bullet} + H_2O_{gas} + O_o^{\times} \Leftrightarrow 2(OH)_o^{\bullet}, \qquad (1)$$

where $V_o^{\bullet\bullet}$ is the oxygen vacancy, $(OH)_O^{\bullet}$ is the hydroxyl group in the oxygen position, and $O_o^{\times}$ is the oxygen atom in the oxygen position. The possibility of using such materials as an electrolyte for medium-temperature fuel cells (the most promising among known electrochemical generators due to high efficiency, the absence of precious metals in their design, as well as minimal requirements for the composition of hydrogen-containing gas) stimulated intensive research of perovskites as high-temperature protonics [5–8]. The main direction in the development of such electrolytes is multi-cationic doping or modification of basic oxide compounds in order to: 1) reduce the temperature at which the electrolyte has sufficient ionic conductivity, 2) reduce the sintering temperature of the electrolyte material powders to a gas-dense state, 3) increase the mechanical strength of the electrolyte ceramics, 4) improve thermomechanical properties, in particular, suppress phase transitions and change the coefficient of thermal expansion (CTE) to achieve its proximity to the CTE of other components of electrochemical devices, 5) increase the chemical resistance of the electrolyte in relation to interaction with the gaseous medium and with other components of electrochemical devices, 6) reduce cost [9, 10].

Later, other structural types based on complex oxides were discovered, for which the process of proton incorporation occurs without the introduction of an acceptor dopant. For example, since 2019, phases based on $BaLaInO_4$, $SrLaInO_4$, $BaNdInO_4$, $BaNdScO_4$ and $BaLaInO_4$ [11–20] with the Ruddlesden-Popper structure have been intensively studied as representatives of a new class of proton conductors [14]. For such structures, the strategy for optimizing their proton-conducting properties is based on changing

[1] Based on the materials of the report at the 17th International Meeting "Fundamental and applied problems of solid state ionics", Chernogolovka, June 16–23, 2024.

the size of the rock salt block, since during hydration it is possible to increase the coordination number of the cation standing in the rock salt block with the participation of OH groups in its coordination.

For a more complex structural type, hexagonal perovskite-like compounds built on a block principle from fragments of various structural types, high-temperature proton transport was also discovered in the 1920s, and super proton conduction can be realized for such phases over a wide temperature range. For example, the phase of the composition $Ba_5Er_2Al_2ZrO_{13}$ exhibited proton conductivity of ~10^{-3} ohms^{-1}×cm^{-1} at 300 °C [21]. Structural analogues with different natures of the M^{3+}-cation with the general formula $Ba_5M_2Al_2ZrO_{13}$ (M=Gd-Lu, Y, Sc) are described in [22]. The structure of such phases can be represented as a result of the fusion of oxygen-deficient $Ba_2M^{3+}AlO_5$ and $BaZrO_3$ perovskite blocks [22]. The conductivity of the phases $Ba_5M_2Al_2ZrO_{13}$ (M=Dy, Er, Tm, Yb, and Lu) was measured in [21]. It was shown that in the temperature range of 400–800 °C in humid air, the differences in conductivities reach one order of magnitude, depending on the nature of the M^{3+}-cation. The conductivity increased in the range Lu<Tm<Dy<Yb≈Er. However, no analysis of the effect of the nature of REE on ion transport processes was carried out.

The interest in such phases is also caused by their high chemical resistance to atmospheres containing CO_2. For example, it was reported that a compound with a hexagonal $Ba_5Er_2Al_2SnO_{13}$ structure maintained phase stability after prolonged heat treatment at 600 °C in a carbon dioxide atmosphere [23].

For such structures, the process of proton incorporation (i.e., OH groups) is ensured by the presence of coordination-unsaturated Ba^{2+} polyhedra in the oxygen-deficient *h′*-layers, which have the shape of a nine-sided [BaO_9]. In such hexagonal *h′*-layers, aluminum tetrahedra connect through the vertex, forming the Al_2O_7 grouping, while oxygen-deficient BaO_2 layers (is the unoccupied oxygen position) are formed, alternating with oxygen-complete BaO_3 layers. Accordingly, coordination-unsaturated Ba^{2+} polyhedra are able to increase the coordination number with the participation of OH groups in their coordination.

Within the framework of quasi-chemical formalism, the process of dissociative dissolution of water vapor in the structure of hexagonal perovskites, by analogy with other complex oxides containing structural oxygen vacancies, can be described as follows:

$$(V_O^s)^\times + O_o^\times + H_2O \Leftrightarrow (OH)_o^\bullet + (OH)_i, \qquad (2)$$

where $(V_O^s)^\times$ is the structural oxygen vacancy, $O_o^\times$ is the oxygen atom in the regular position, $(OH)_O^\bullet$ is the hydroxyl group in the oxygen position, and $(OH)_i$ is the hydroxyl group in place of the structural oxygen vacancy. Oxygen-ion and proton transport in hexagonal perovskite of the composition $Ba_5In_2Al_2ZrO_{13}$ was studied in more detail [24–27]. When studying the effect of various types of substitutions on ionic (O2-, H^+) transport, it was shown that for such structures, acceptor doping is not an effective strategy for significantly increasing ionic conductivity, compared with classical ABO_3 perovskites. At the same time, the isovalent doping method, which makes it possible to modify geometric characteristics, leads to an increase in ionic conductivity.

In addition to the compounds with the coherent fusion structure described above, high-temperature proton transport has recently been discovered in hexagonal perovskite $Ba_7In_6Al_2O_{19}$ [28]. The structure of this phase is also based on the block principle of fragments of various structural types, it can be represented as coalescence along the axis from two blocks Ba_2InAlO_5 and one block $Ba_3In_4O_9$. The $Ba_7In_6Al_2O_{19}$ phase was characterized by higher values of ionic (O^{2-}, H^+) conductivities than $Ba_5In_2Al_2ZrO_{13}$. However, there is no information in the literature about the possible types of substitutions in this phase and their effect on transport properties. In addition, it is of interest to compare the isovalent substitution method for two phases $Ba_7In_6Al_2O_{19}$ and $Ba_5In_2Al_2ZrO_{13}$, characterized by the coalescence of identical Ba_2InAlO_5 blocks (oxygen-deficient block), but differing in $Ba_3In_4O_9$ blocks (cation-deficient perovskite) and $BaZrO_3$ (complete perovskite).

For this purpose, in this work, the synthesis of the Y^{3+}-doped phase of the composition $Ba_7In_{5.9}Y_{0.1}Al_2O_{19}$ was carried out, its conductivity was studied as a function of temperature and pO_2 in atmospheres of different humidity, and the ability to hydrate was proved by thermogravimetry. The data obtained were compared with the Y^{3+}-doped phase of $Ba_5In_2Al_2ZrO_{13}$ [24–27].

EXPERIMENTAL PART

Samples of the compositions $Ba_7In_6Al_2O_{19}$ and $Ba_7In_{5.9}Y_{0.1}Al_2O_{19}$ were obtained by solid-phase synthesis from pre-dried $BaCO_3$ (operating hours 7–4), Al_2O_3 (operating hours 12–3), In_2O_3 (operating hours 12–3). The synthesis was carried out in air according to the scheme: 800 °C, 24 h.; 1000 °C, 24 h.; 1100 °C, 72 h., after each stage, grinding was carried out in an agate mortar in an ethyl alcohol medium.

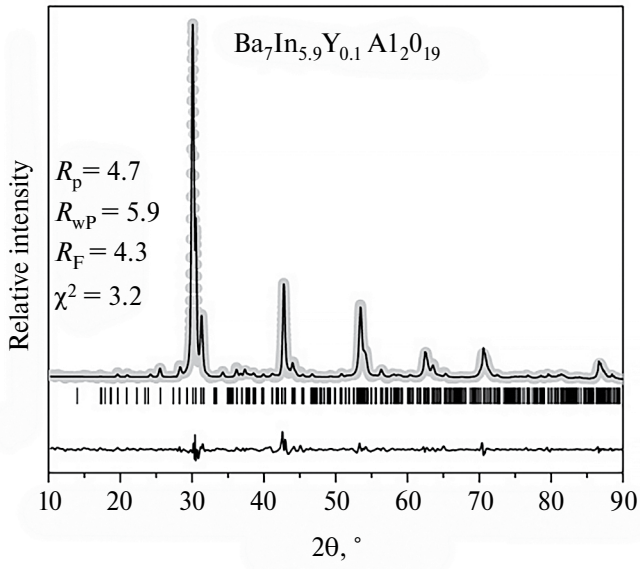

Fig. 1. Experimental, calculated, and differential radiographs, as well as the angular positions of the reflexes of the $Ba_7In_{5.9}Y_{0.1}Al_2O_{19}$ sample.

To measure the electrical properties, the samples were prepared in the form of tablets, sintering was carried out at a temperature of 1300 °C for 48 hours. The values of the relative density of the ρ_{rel} of the obtained ceramic samples were determined as the ratio of the geometric density to the X-ray density. For the studied phases, they were: ρ_{rel} = 82.7% for $Ba_7In_6Al_2O_{19}$ and ρ_{rel} = 81.6% for $Ba_7In_{5,9}Y_{0,1}Al_2O_{19}$. The palladium-silver electrodes were fired at a temperature of 900 °C for 3 hours.

X-ray analysis was performed on an ARL EQUINOX 3000 diffractometer (ThermoFisherScientific, USA) in CuK_α radiation at a tube voltage of 40 kV and a current of 40 mA. The imaging was carried out in the range of 2θ = 10°–90° with a step of 0.024° and an exposure of 1 s per point. The lattice parameters were calculated using the FullProf program.

The surface morphology of the powder samples and the local chemical composition were studied using a VEGA3 scanning electron microscope (SEM) (Tescan, Czech Republic) with an X-ray energy dispersion microanalyzer AztecLiveStandardUltimMax 40 (Oxford Instruments, Great Britain). The detection limit at normal energies (5–20 kV) was ~0.5 at.%, the concentration measurement error was ± 2%. The survey was carried out at a voltage of 20 kV in secondary and back-reflected electrons.

Hydrated sample forms were prepared for thermogravimetric (TG) measurements. The samples were previously calcined at a temperature of 1100 °C in a dry nitrogen atmosphere in order to remove possible carbonation products. The calcined samples were then slowly cooled in an atmosphere of moist nitrogen ($pH_2O = 1.92 \cdot 10^{-2}$ atm) to 200 °C. Nitrogen humidity was set according to the procedure described below for measuring electrical conductivity. Thus, the lower hydration temperature provided conditions that excluded the appearance of adsorption moisture in the sample. Next, thermogravimetric analysis of the hydrated samples was performed on TG STA 409 PC thermal balance (Netzsch, Germany). The measurements were carried out in the temperature range of 25–1000 °C with a heating rate of 10 °/min in an argon atmosphere.

The study of electrical conductivity was carried out by the electrochemical impedance method in the frequency range 10^2–3×10^6 Hz using the Elins Z-3000X impedance parameter meter (Elins LLC, Russia). All electrochemical measurements were performed under equilibrium conditions with T, pH_2O, and pO_2. The volumetric resistance was calculated using Zview software fitting. The values of the electrical conductivity of the samples σ were calculated according to the following formula:

$$\sigma = \frac{l}{SR_{vol}}, \quad (3)$$

where l is the height of the sample, S is the surface area of the sample. The values of the volume resistance R_{vol} were determined from the impedance spectroscopy data. The values of the activation energy E_a and the pre-exponential multiplier A were calculated using the Frenkel equation:

$$\sigma T = A \exp(\frac{-E_a}{kT}), \quad (4)$$

where A is the pre-exponential multiplier, k is the Boltzmann constant, and T is the absolute temperature.

The study of electrical conductivity with varying pO_2 was carried out in the oxygen partial pressure range of 10^{-18}–0.21 atm. The oxygen pressure was set and monitored using an "oxygen pump" and an oxygen partial pressure sensor made from a stabilized solid electrolyte based on ZrO_2. The oxygen partial pressure values were monitored by the Zirconia-M regulator (Research Technologies LLC, Russia).

The electrical conductivity of the studied phases was studied in atmospheres of different humidity. A moist atmosphere was obtained by bubbling gas at room temperature sequentially through distilled water and a saturated solution of potassium bromide KBr ($pH_2O = 1.92 \times 10^{-2}$ atm). The dry atmosphere was set by gas circulation through powdered phosphorus oxide P_2O_5 ($pH_2O = 3.5 \times 10^{-5}$ atm). In addition, to prevent possible carbonation of ceramics, preliminary removal of CO_2

Table 1. Values of parameters, volume and free volume of unit cells for phases $Ba_7In_6Al_2O_{19}$ and $Ba_7In_{5.9}Y_{0.1}Al_2O_{19}$

Phase	a, Å	c, Å	V, Å^3	$V_{св}$, Å^3
$Ba_7In_6Al_2O_{19}$	5.921(2)	37.717(4)	1145.2(3)	481.3(6)
$Ba_7In_{5.9}Y_{0.1}Al_2O_{19}$	5.935(7)	37.736(8)	1151.4(4)	487.3(9)

carbon dioxide from the air was carried out, for a wet atmosphere using a 20% NaOH solution, for a dry atmosphere using the Ascarite reagent. The humidity of the gases was controlled by a HIH-4000 gas humidity sensor (Honeywell, USA) of a capacitive type, which allows measurements of relative humidity from 0 to 100%. In addition to the sensor element, an electrical circuit is located on the sensor substrate, providing signal conversion, amplification and linearization. The sensor output is a function of voltage, ambient temperature, and humidity. The sensor was directly connected to the microcontroller to process the linear voltage signal.

RESULTS AND DISCUSSION

Phase analysis and morphological assessment

According to X-ray phase analysis, the $Ba_7In_6Al_2O_{19}$ matrix compound and the $Ba_7In_{5.9}Y_{0.1}Al_2O_{19}$ phase were obtained as single-phase and were characterized by a hexagonal structure (spatial group $P6_3/mmc$). Fig. 1 shows an example of X-ray data processing by the Rietveld method of full-profile analysis for a sample of the composition $Ba_7In_{5.9}Y_{0.1}Al_2O_{19}$.

When yttrium was introduced, the parameters of unit cells, volume, and free volume increased, due to the large value of the ionic radius of yttrium ($r_{Y^{3+}}$ = 0.90 Å) compared with indium ($r_{In^{3+}}$=0.80 Å) [29]. Table 1 shows the corresponding parameter values.

SEM images of the chipped surface of the ceramic and powder sample $Ba_7In_{5.9}Y_{0.1}Al_2O_{19}$ obtained in secondary electrons are shown in Fig. 2*a* and 2*b*, respectively. For the powder sample (Fig. 2*b*), small rounded crystallites with sizes of 2–5 μm were observed, partially agglomerated into larger irregularly shaped grains, the sizes of which averaged 10–12 μm. The crystalline grains of both the initial compound and the studied yttrium-substituted phase had approximately the same size and shape. Thus, the introduction of yttrium into the initial matrix did not affect the size and shape of the crystallites. No crystalline grains corresponding to any impurity phases were found in the images of all the samples studied. The chipped surface of the ceramic sample is represented by irregularly shaped fused grains, with individual pores visible (Fig. 2*a*). The cationic composition of the obtained samples was determined by the analysis of energy-dispersive X-ray spectroscopy (EDX)

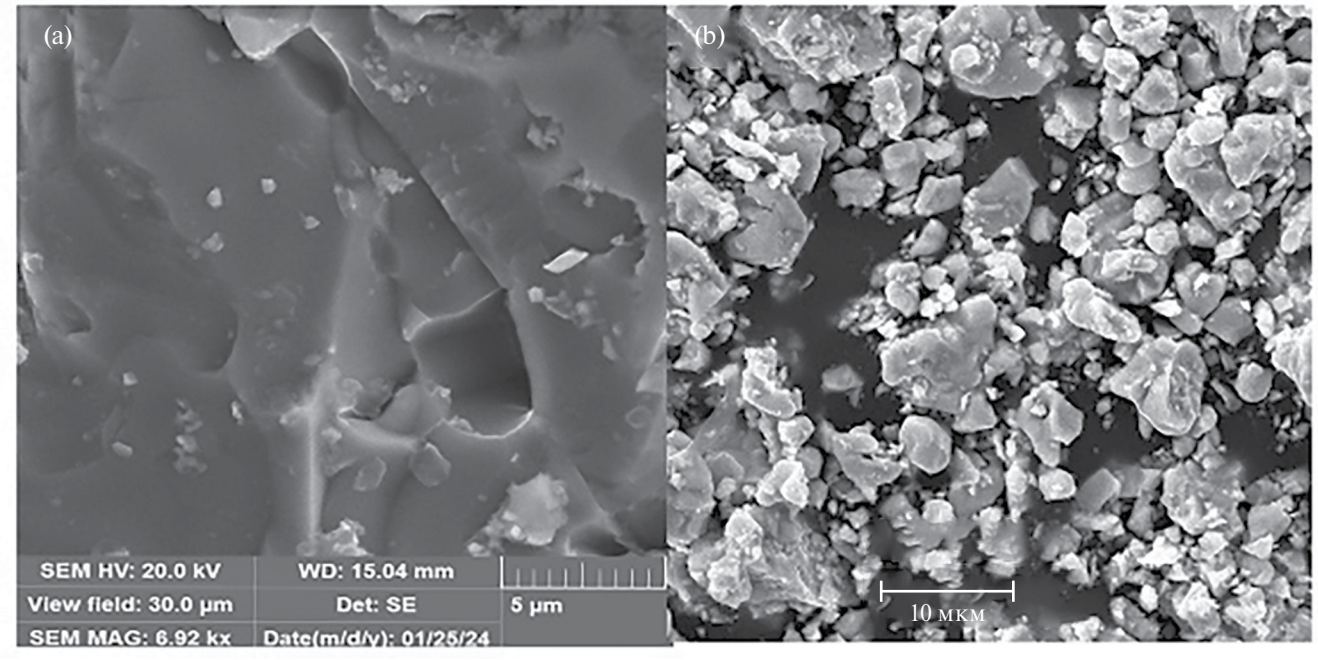

Fig. 2. SEM images of the surface of the chipped ceramic (a) and powder (b) samples $Ba_7In_{5.9}Y_{0.1}Al_2O_{19}$.

Table 2. Elemental analysis data based on the results of EDX studies for ceramic samples of the composition $Ba_7In_6Al_2O_{19}$ and $Ba_7In_{5.9}Y_{0.1}Al_2O_{19}$

Phase	at.% (theoretical)				at.% (experimental)			
	Ba	In	Y	Al	Ba	In	Y	Al
$Ba_7In_6Al_2O_{19}$	46.7	40.0	0.0	13.3	45.8	38.6	0	15.6
$Ba_7In_{5.9}Y_{0.1}Al_2O_{19}$	46.7	39.3	0.7	13.3	45.5	38.0	0.7	15.8

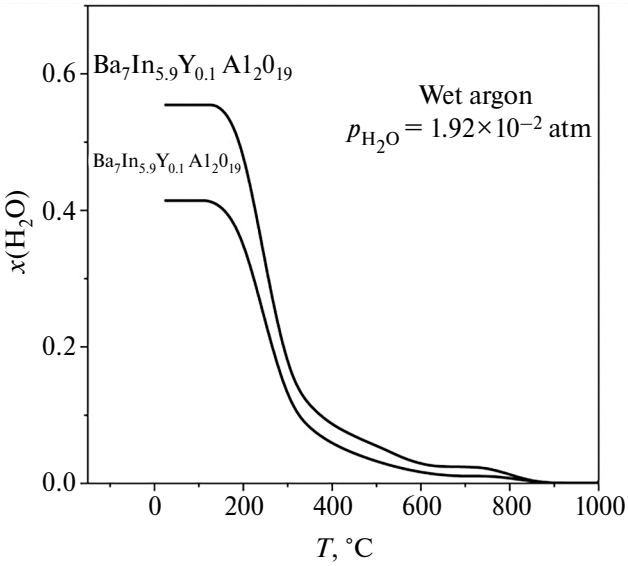

Fig. 3. TG curves of hydrated samples $Ba_7In_6Al_2O_{19}{\cdot}xH_2O$ and $Ba_7In_{5.9}Y_{0.1}Al_2O_{19}{\cdot}xH_2O$.

on the chips of ceramic samples. The experimentally obtained values are consistent with the theoretical ones, the difference in the values of the cation content did not exceed 2–2.5%, which makes it possible to conclude that the elemental composition was preserved for all the phases obtained (Table 2).

Thermal properties

Fig. 3 shows the results of thermal analysis of the hydrated phases of the compositions $Ba_7In_6Al_2O_{19}{\cdot}xH_2O$ and $Ba_7In_{5.9}Y_{0.1}Al_2O_{19}{\cdot}xH_2O$. The results are presented as moles of water (degree of hydration xH_2O) per formula unit. A similar type of TG curves was observed for both phases: mass changes occurred in the temperature range of 200–950 °C, while the main mass change occurred in the temperature range of 200–400 °C, and mass stabilization of the samples was observed above 950 °C.

The experimentally obtained values of the degree of hydration of the Y-doped phase (0.55 mol H_2O) were higher than for the matrix phase $Ba_7In_6Al_2O_{19}$ (0.41 mol H_2O). Since the isovalent doping method was used in the work, the increase in the degree of hydration is not associated with any additional disordering, but is caused by a change in the geometric characteristics of the unit cell. This behavior during hydration is due to the specifics of the structure of the phases under study, namely, the presence of oxygen-deficient BaO_2 layers in the hexagonal *h'* -block, respectively, an increase in the size of this block during doping makes it possible to incorporate large concentrations of OH groups.

It can be concluded that for block-type structures containing coordination-unsaturated polyhedra of large-sized cations, the strategy of increasing the size of such blocks is favorable for accommodating more OH groups coordinating these cations. Similar trends, such as an increase in the degree of hydration with an increase in the geometric parameters of the unit cell (or the volume of the unit cell), were observed for hydrated phases with the Ruddlesden–Popper $BaLaInO_4$ structure [30], and for hexagonal perovskites $Ba_5In_2Al_2ZrO_{13}$ [25–27].

Electrical properties

Fig. 4 shows examples of the evolution of impedance hodographs in Nyquist coordinates with temperature variation in dry (Fig. 4*a*) and humid (Fig. 4*b*) air.

As can be seen, the general appearance of the impedance spectra was similar – a semicircle emanating from the origin was observed in the region of the main frequencies under study, and an asymmetry of its right side was observed in the region of lower frequencies, which is the result of overlap with the second relaxation process. The capacity values obtained for the first semicircle were 10^{-12}–10^{-11} F, which corresponds to the volume contribution for the second, 10^{-10}–10^{-9}F, which corresponds to the contribution of grain boundaries. Therefore, the processing in the ZView program was carried out in accordance with the equivalent scheme shown in Fig. 4*b*. A small part of the third semicircle was observed in the low frequency region, which is typical for electrode processes. Further in the text, the volume resistance values obtained by extrapolating the corresponding semicircle to the abscissa axis (processing in ZView) will be discussed.

The electrical conductivity of all samples was studied over a wide range of oxygen partial pressures to determine the contributions of partial conductivities. Fig. 5 shows typical dependences. As can be seen,

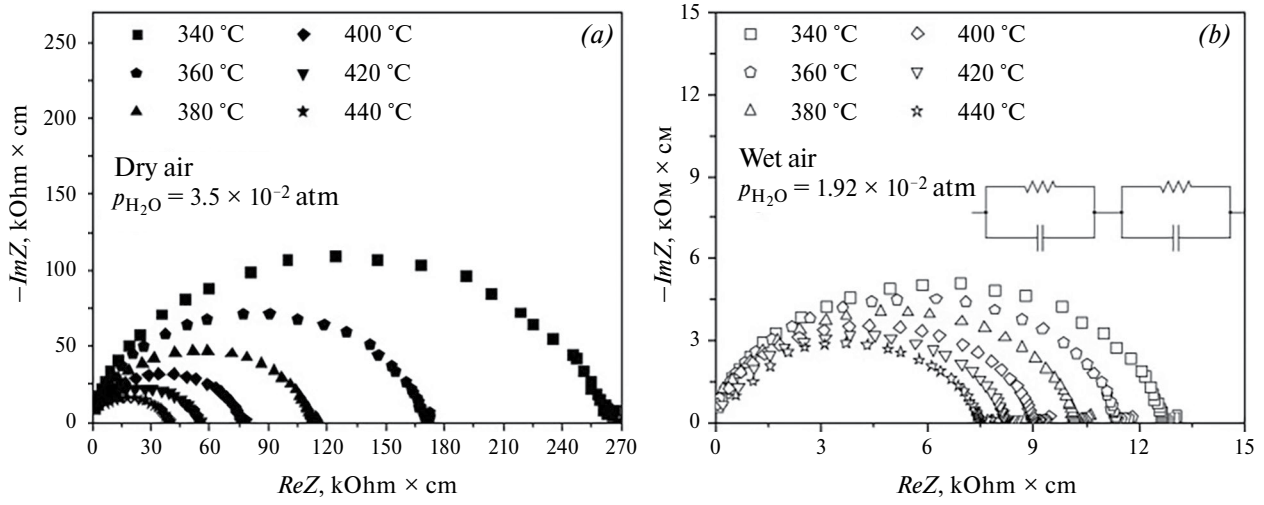

Fig. 4. Evolutions of impedance hodographs with temperature variation in dry (a) and moist (b) air for $Ba_7In_{5.9}Y_{0.1}Al_2O_{19}$.

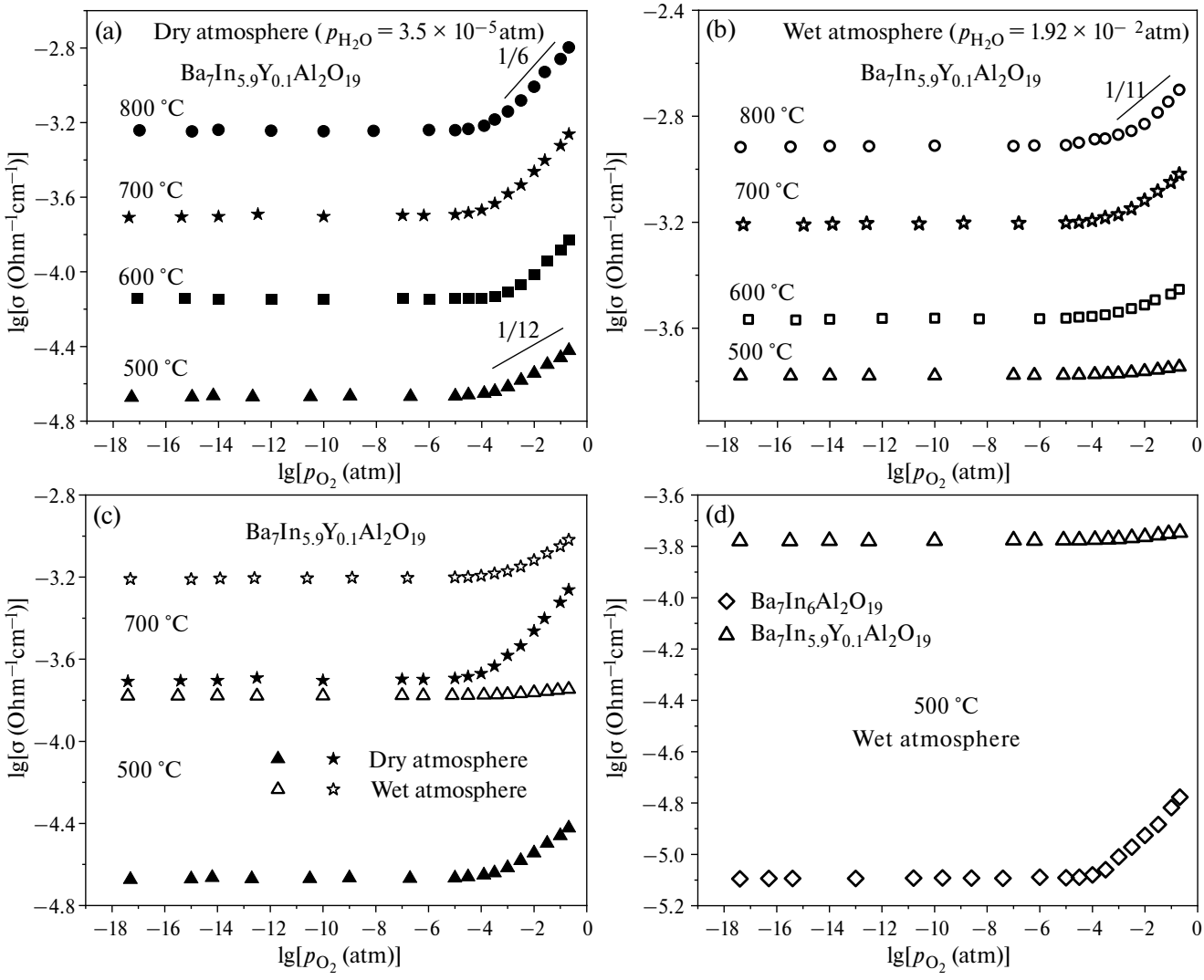

Fig. 5. Dependences of electrical conductivity on the partial pressure of oxygen of the $Ba_7In_{5.9}Y_{0.1}Al_2O_{19}$ phase in dry ($pH_2O = 3.5 \cdot 10^{-5}$ atm) (*a*) and wet ($pH_2O = 1.92 \cdot 10^{-2}$ atm) (*b*) atmospheres, as well as comparison of isotherms in dry and wet atmospheres (*c*) and comparison of with an undoped phase of $Ba_7In_6Al_2O_{19}$ at 500 °C (*d*).

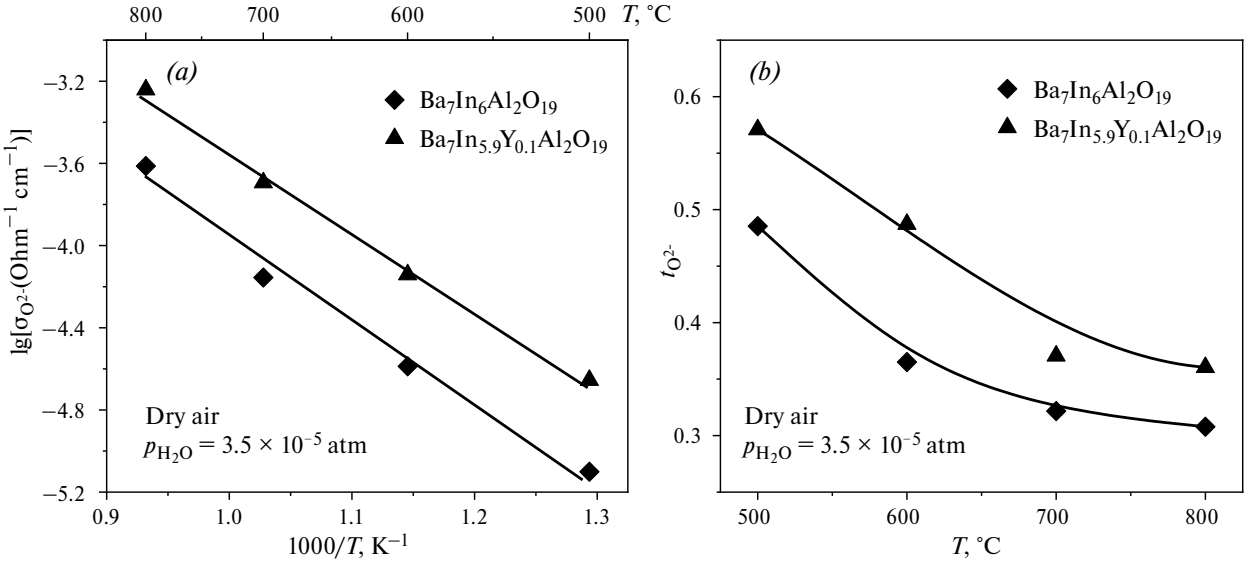

Fig. 6. Temperature dependences of oxygen-ion conductivity (*a*) and oxygen-ion transfer numbers (*b*) for $Ba_7In_6Al_2O_{19}$ and $Ba_7In_{5.9}Y_{0.1}Al_2O_{19}$ in dry air atmosphere ($pH_2O = 3.5\times10^{-5}$ atm).

the conductivity (Fig. 5*a*) in a wide range of partial pressures of oxygen pO_2 (10^{-18}–10^{-5} atm) remains constant – this is an electrolytic region where atomic defects are dominant. Taking into account the crystallochemical features of the $Ba_7In_6Al_2O_{19}$ structure (the presence of oxygen-deficient layers), the mechanism of oxygen-ion conductivity can be represented as an exchange of lattice oxygen and oxygen vacancies. At the same time, oxygen vacancies in such structures are nodes of the crystal lattice that are not occupied by atoms, i.e., a structural defect. Therefore, from a quasi-chemical point of view, this process can be described as follows:

$$O_O^{\times} + (V_O^s)^{\times} \leftrightarrow V_O^{\bullet\bullet} + O_i'', \qquad (5)$$

where $(V_O^S)^{\times}$ is the structural oxygen vacancy, $V_O^{\bullet\bullet}$ is the oxygen vacancy formed in place of the departed oxygen, $O_O^{\times}$ is oxygen in the oxygen position, O_i'' is the oxygen ion in the structural oxygen vacancy.

With an increase in the partial pressure of oxygen ($pO_2 > 10^{-5}$atm), the electrical conductivity begins to increase, which indicates the appearance of a contribution of hole conductivity:

$$(V_O^S)^{\times} + 1/2O_2 \leftrightarrow O_i'' + 2h^{\bullet}. \qquad (6)$$

Accordingly, total conductivity can be represented as the sum of the ionic conductivity, independent of pO_2, and the hole conductivity, for which the slope is $d\lg\sigma_h/d\lg pO_2 = 1/4$:

$$\sigma_{tot} = \sigma_{ion} + \sigma_h = \sigma_{ion} + KpO_2^{1/4}, \qquad (7)$$

where σ_{tot}, σ_{ion}, and σ_h are, respectively, the total, ionic, and hole conductivities, and K is a constant.

It should be noted that the general form of the $\lg\sigma_{tot}$–$\lg pO_2$ dependences for the studied phases had similar features: for dry atmosphere in the region of high partial pressures of oxygen pO_2, the positive slope of the total conductivity decreased with the decreasing temperature, which indicates an increase in the contribution of ionic conductivity. Thus, the values of oxygen-ion conductivity $\sigma_{O^{2-}}$ (conductivity in the plateau region) were obtained from the experimental $\lg\sigma$-$\lg pO_2$ data and the ion transfer numbers were calculated as $t_{O^2} = \sigma_{O^{2-}}/\sigma_{tot}$.

Fig. 6 shows the temperature dependences of the oxygen-ion conductivity of the studied phases. All dependences in the Arrhenius coordinates were characterized by a linear form. The calculated values of the activation energy E_a of oxygen-ion conductivity and the pre-exponential multiplier A in accordance with equation (4) are shown in Table 3.

As can be seen, the values of oxygen-ion conductivity increased for the yttrium-doped phase. At the same time, the activation energy decreased and the pre-exponential multiplier increased, both factors being favorable in terms of increasing oxygen-ion conductivity. The observed trends may be due to an increase in the volume (as well as the free volume) of the unit cell as a result

Table 3. Values of the activation energy of oxygen-ion conductivity and the pre-exponential multiplier for the phases of the composition $Ba_7In_6Al_2O_{19}$ and $Ba_7In_{5.9}Y_{0.1}Al_2O_{19}$

Phase	E_a, Ev	A, $Ohm^{-1}S^{-1}K$
$Ba_7In_6Al_2O_{19}$	0.85±0.01	2711±321
$Ba_7In_{5.9}Y_{0.1}Al_2O_{19}$	0.79±0.01	4374±518

of the substitution of indium for yttrium that is larger in size. As the geometric parameters increased, the values of the ion jump length increased, which was confirmed by an increase in the values of the pre-exponential multiplier. This fact is due to the proportionality of the pre-exponential factor A to the square of the jump length, in accordance with the formula

$$A = Gq^2a^2\nu_o/k, \quad (8)$$

where G is the geometric multiplier, q is the charge, a is the ion jump length, ν_o is the jump frequency, and k is the Boltzmann constant [8]. Accordingly, an increase in the lattice parameters will correlate with an increase in the jump length. Also the data in Table 3 demonstrates the often experimentally observed relationship between the activation energy and the pre-exponential multiplier. With an increase in the lattice parameters (respectively, the interatomic distances), the interaction forces of ions weaken, and their migration requires less energy, respectively, the migration energy of oxygen ions decreases and, as a result, the conductivity increases [31]. Indeed, the activation energy of oxygen-ion transfer determined from temperature dependences, which directly reflects the migration energy, decreases with the increasing lattice parameters (Tables 1, 3).

A parameter such as the free volume of a unit cell, introduced in [32] as a volume not occupied by atoms, allows us to estimate the free space for atomic migration, and its increase with the introduction of yttrium is also a favorable factor in increasing ionic conductivity.

The oxygen-ion transfer numbers (Fig. 6*b*) reflect the trends discussed above: doping led to an increase in oxygen-ion transfer numbers, with decreasing temperature the proportion of oxygen-ion transfer increased, and below 500 °C ion transport dominated.

A comparison of the oxygen-ion conductivities of the studied phase with hexagonal perovskite $Ba_5In_{1.9}Y_{0.1}Al_2ZrO_{13}$, described earlier in [24, 26], is shown in Fig. 7. As can be seen, the studied phase of $Ba_7In_{5.9}Y_{0.1}Al_2O_{19}$ exhibits more significant values of oxygen-ion conductivity than $Ba_5In_{1.9}Y_{0.1}Al_2ZrO_{13}$, which demonstrates the effect of cation deficiency in $Ba_7In_{5.9}Y_{0.1}Al_2O_{19}$, which, accordingly, is accompanied by large values of free migration volume, contributing to facilitated ion transport.

A similar set of studies was conducted for the humid air atmosphere ($pH_2O=1.92\times10^{-2}$ atm). The presence of oxygen vacancies in the structure of the phases $Ba_7In_6Al_2O_{19}$ and $Ba_7In_{5.9}Y_{0.1}Al_2O_{19}$ causes the appearance of proton defects in the interaction of samples with the water-containing gas phase and, as a result, the appearance of proton conductivity. Fig. 5*b* demonstrates the most typical behavior

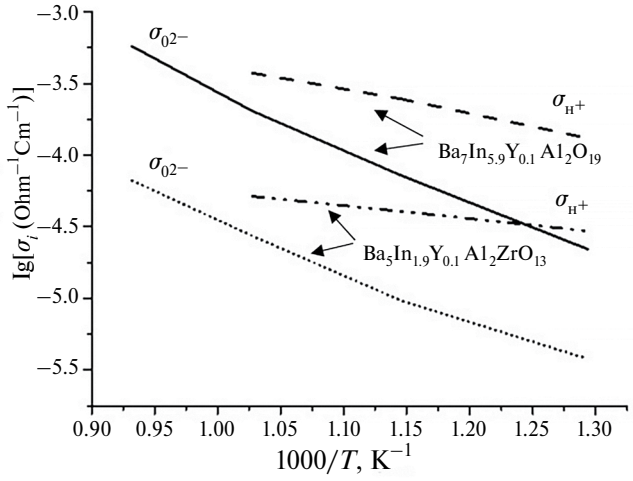

Fig. 7. Temperature dependences of the proton and oxygen-ion conductivities $Ba_7In_{5.9}Y_{0.1}Al_2O_{19}$ and $Ba_5In_{1.9}Y_{0.1}Al_2ZrO_{13}$.

of the conductivity of proton conductors with a change in atmospheric humidity. The following general patterns can be distinguished due to the introduction of water into the structure and the appearance of the proton component of conductivity:

— in a humid atmosphere, the total electrical conductivity increased compared to the values obtained in dry conditions (most significantly at temperatures below 600 °C), Fig. 5*c*;

— with a decrease in temperature, the area of the plateau of the $\lg\sigma_{tot}-\lg pO_2$ dependences expanded, the slope in the $pO_2 \geqslant 10^{-4}$ atm region became more shallow (Fig. 5*b*), as a result of an increase in the ionic conductivity contribution; below 500 °C in the entire studied area, the pO_2Y^{3+}-doped sample showed the dominant ion transport, Fig. 5*d*.

From the point of view of the quasi-chemical approach, the process of interaction of water vapor with structural oxygen vacancies (as an alternative to equation (2)) can be represented, in particular, as follows:

$$H_2O + 2O_O^{\times} + (V_O^S)^{\times} \rightarrow 2OH_O^{\bullet} + O_i^{''}. \quad (9)$$

According to this equation, the oxygen of the water molecule is embedded in the structural oxygen vacancy $(V_O^S)^{\times}$, protons are localized on regular oxygen nodes, forming the group $OH_O^{\bullet}$. Since the structural vacancy is considered as a neutral defect, i.e., it is identical to the free interstitial position, the additional oxygen ion embedded in such a position has the same effective charge as the interstitial oxygen ion $O_i^{''}$.

The value of proton conductivity was estimated from the experimental $\lg\sigma$-$\lg pO_2$ data on the difference in the values of ionic conductivity in wet and dry atmospheres. The temperature dependences of the proton electrical conductivities

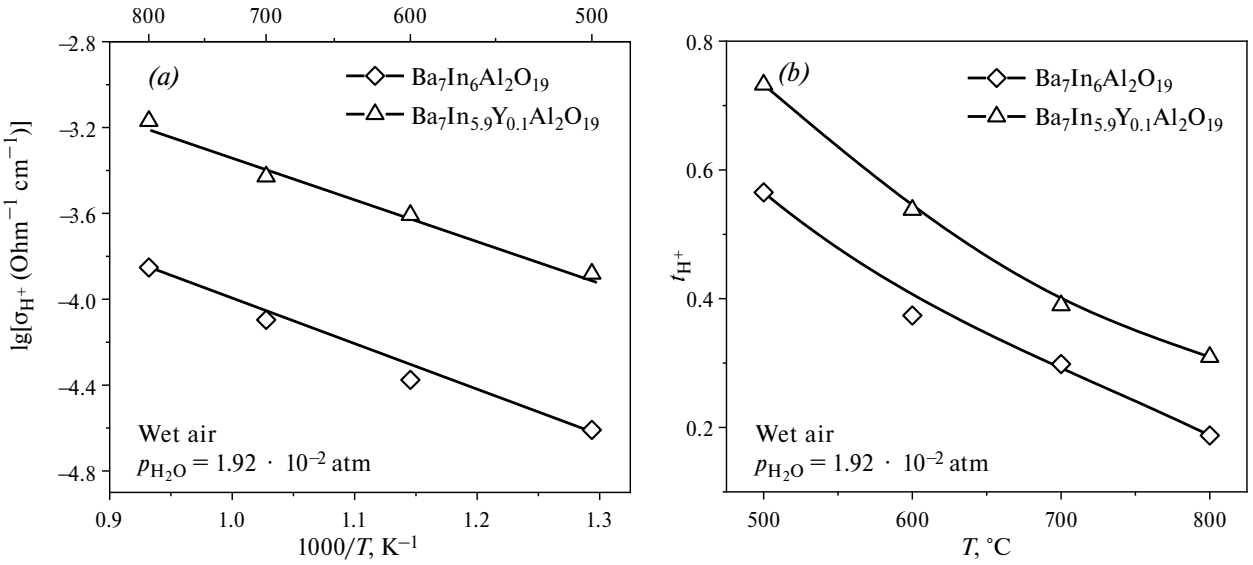

Fig. 8. Temperature dependences of proton conductivity and proton transfer numbers for phases $Ba_7In_6Al_2O_{19}$ and $Ba_7In_{5.9}Y_{0.1}Al_2O_{19}$.

are shown in Fig. 8 for the phases $Ba_7In_6Al_2O_{19}$ and $Ba_7In_{5.9}Y_{0.1}Al_2O_{19}$. Throughout the studied temperature range, an increase in proton conductivity values was observed for the yttrium-doped phase, while the activation energy values decreased to 0.40 eV compared with 0.47 eV for the undoped phase. The increase in proton conductivity for the yttrium-doped phase may be the result of higher proton concentrations, which is confirmed by TG studies. The temperature dependences of the proton transfer numbers $Ba_7In_{5.9}Y_{0.1}Al_2O_{19}$ (Fig. 8*b*) confirm the dominant proton transport below 500 °C.

A comparison of the temperature dependences of the proton conductivities of the two Y-doped phases $Ba_7In_{5.9}Y_{0.1}Al_2O_{19}$ and $Ba_5In_{1.9}Y_{0.1}Al_2ZrO_{13}$ is shown in Fig. 7. It can be seen that for both oxygen-ion conductivity and proton conductivity, higher values were observed for the $Ba_7In_{5.9}Y_{0.1}Al_2O_{19}$ phase. That is, we can state the influence of the dynamics of the oxygen sublattice on proton transport. The symbatic behavior of oxygen-ion and proton conductivities, demonstrating the effect of the state of the oxygen sublattice on the formation of proton conductivity, was previously described for acceptor-doped perovskites and confirmed for numerous compounds. Obviously, such general patterns are typical for various structural types of proton-conducting complex oxides.

Thus, it can be concluded that the strategy of doping hexagonal perovskite $Ba_7In_6Al_2O_{19}$ with yttrium is promising, as it allows increasing proton conductivity. Further study of the effect of doping on the transport properties of $Ba_7In_6Al_2O_{19}$ may be related to studies of a wide concentration range of Y^{3+} dopant, which can optimize proton transport to a greater extent, and also to the study of concentration dependences.

CONCLUSION

Hexagonal perovskite $Ba_7In_{5.9}Y_{0.1}Al_2O_{19}$ was obtained by solid-phase synthesis. The introduction of yttrium into the indium sublattice led to an increase in the unit cell parameters (a = 5.935(7) Å, c = 37.736(8) Å) compared with the undoped $Ba_7In_6Al_2O_{19}$ phase (a = 5.921(2) Å, c = 37.717(4) Å). Isovalent doping led to an increase in the degree of hydration to x=0.55 mol H_2O (compared with 0.41 mol H_2O for the undoped phase), as a result of an increase in lattice parameters and the possibility of incorporating large concentrations of OH groups into oxygen-deficient blocks. The increase in interatomic distances also contributed to an increase in oxygen-ion transport. The $Ba_7In_{5.9}Y_{0.1}Al_2O_{19}$ phase is capable of proton conduction in atmospheres with high partial pressures of water vapor ($pH_2O = 1.92 \cdot 10^{-2}$ atm), proton transfer became dominant below 500 °C.

The ionic (O^{2-}, H^+) conductivities of the studied phase $Ba_7In_{5.9}Y_{0.1}Al_2O_{19}$ and hexagonal perovskite $Ba_5In_{1.9}Y_{0.1}Al_2ZrO_{13}$, which does not contain barium vacancies, are compared. It has been established that cationic deficiency contributes to facilitated ion transport as a result of a greater free migration volume.

FUNDING

The work was supported by the Russian Science Foundation and the Government of the Sverdlovsk Region No. 24–13–20026, https://rscf.ru/project/24-13-20026/.

CONFLICT OF INTEREST

The authors declare that they have no conflict of interest.

REFERENCES

1. Takahashi, T. and Iwahara, H., Solid-state ionics: Protonic conduction in perovskite-type oxide solid solution, *Rev. Chem. Mineral*, 1980, vol. 17, no. 4, p. 243.
2. Iwahara, H., Esaka, T., Uchida, H., and Maeda, N., Proton conduction in sintered oxides and its application to steam electrolysis for hydrogen production, *Solid State Ionics,* 1981, vol. 3, no. 4, p. 359.
3. Uchida, H., Maeda, N., and Iwahara, H., Steam concentration cell using a high temperature type proton conductive solid electrolyte, *J. Appl. Chem.*, 1982, vol. 12, p. 645.
4. Iwahara, H., Uchida, H., and Maeda, N., High temperature fuel and steam electrolysis cells using proton conductive solid electrolytes, *J. Power Sources*, 1982, vol. 7, no. 3, p. 293.
5. Danilov, N., Lyagaeva, J., Vdovin, G., and Medvedev, D., Multifactor performance analysis of reversible solid oxide cells based on proton-conducting electrolytes, *Appl. Energy* 2019, vol. 237, p. 924.
6. Tarutin, A., Kasyanova, A., Lyagaeva, J., Vdovin, G., and Medvedev, D., Towards high-performance tubular-type protonic ceramic electrolysis cells with all-Ni-based functional electrodes, *J. Energy Chem.*, 2020, vol. 40, p. 65.
7. Medvedev, D.A., Current drawbacks of proton–conducting ceramic materials: How to overcome them for real electrochemical purposes, *Curr. Opin. Green Sustain. Chem.*, 2021, vol. 32, p. 100549.
8. Yaroslavtsev, A.B., Solid electrolytes: main prospects of research and development, *Russ. Chem. Rev.*, 2016, vol. 85, no. 11, p. 1255.
9. Kochetova, N., Animitsa, I., Medvedev, D., Demin, A., and Tsiakaras, P., Recent activity in the development of proton-conducting oxides for high-temperature applications, *RSC Adv.*, 2016, vol. 6, p. 73222.
10. Hyodo, J., Tsujikawa, K., Shiga, M., Okuyama, Y., and Yamazaki, Y., Accelerated discovery of proton-conducting perovskite oxide by capturing physicochemical fundamentals of hydration, *ACS Energy Lett.*, 2021, vol. 6, no. 8, p. 2985.
11. Zhou, Y., Shiraiwa, M., Nagao, M., Fujii, K., Tanaka, I., Yashima, M., Baque, L., Basbus, J., Mogni, L., and Skinner, S., Protonic conduction in the $BaNdInO_4$ structure achieved by acceptor doping, *Chem. Mater.*, 2021, vol. 33, p. 2139.
12. Shiraiwa, M., Kido, T., Fujii, K., and Yashima, M., High-temperature proton conductors based on the (110) layered perovskite $BaNdScO_4$, *J. Mat. Chem.* A, 2021, vol. 9, p. 8607.
13. Troncoso, L., Arce, M.D., Fernandez-Diaz, M.T., Mogni, L.V., and Alonso, J.A., Water insertion and combined interstitial-vacancy oxygen conduction in the layered perovskites $La_{1.2}Sr_{0.8-x}Ba_xInO_{4+d}$, *New J. Chem.*, 2019, vol. 43, p. 6087.
14. Tarasova, N., Animitsa, I., Galisheva, A., and Korona, D., Incorporation and conduction of protons in Ca, Sr, Ba-doped $BaLaInO_4$ with Ruddlesden-Popper Structure, *Materials*, 2019, vol. 12, p. 1668.
15. Tarasova, N., Animitsa, I., Galisheva, A., and Pryakhina, V., Protonic transport in the new phases $BaLaIn_{0.9}M_{0.1}O_{4.05}$ (M=Ti, Zr) with Ruddlesden-Popper structure, *Solid State Sci.*, 2020, vol. 101, p. 106121.
16. Tarasova, N., Animitsa, I., and Galisheva, A., Electrical properties of new protonic conductors $Ba_{1+x}La_{1-x}InO_{4-0.5x}$ with Ruddlesden-Popper structure, *J. Solid State Electrochem.*, 2020, vol. 24, p. 1497.
17. Tarasova, N., Galisheva, A., and Animitsa, I., Improvement of oxygen-ionic and protonic conductivity of $BaLaInO_4$ through Ti doping, *Ionics*, 2020, vol. 26, p. 5075.
18. Tarasova, N., Galisheva, A., and Animitsa, I., Ba^{2+}/Ti^{4+}- co-doped layered perovskite $BaLaInO_4$: the structure and ionic (O^{2-}, H^+) conductivity, *Intern. J. Hydrogen Energy,* 2021, vol. 46, p. 16868.
19. Tarasova, N., Galisheva, A., Animitsa, I., and Korona, D., Hydration and the state of oxygen–hydrogen groups in the complex oxide $BaLaIn0_{.9}Nb_{0.1}O_{4.1}$ with the Ruddlesden–Popper structure, *Russ. J. Phys. Chem. A*, 2020, vol. 94, p. 818.
20. Tarasova, N., Galisheva, A., Animitsa, I., and Dmitrieva, A., The Effect of donor doping on the ionic (O^{2-}, H^+) transport in novel complex oxides $BaLaIn_{1-x}Nb_xO_{4+x}$ with the Ruddlesden–Popper structure, *Russ. J. Electrochem.*, 2021, vol. 57, p. 962.
21. Murakami, T., Hester, J., and Yashima, M., High proton conductivity in $Ba_5Er_2Al_2ZrO_{13}$, a hexagonal perovskite-related oxide with intrinsically oxygen-deficient layers, *J. Am. Chem. Soc.*, 2020, vol. 142, p. 11653.
22. Shpanchenko, R.V., Abakumov, A.M., Antipov, E.V., Nistor, L., Van Tendeloo, G., and Amelinckx, S., Structural study of the new complex oxides $Ba_{5-y}Sr_yR_{2-x}Al_2Zr_{1+x}O_{13+x/2}$ (R = Gd-Lu, Y, Sc), *J. Solid State Chem.*, 1995, vol. 118, p. 180.
23. Matsuzaki, K., Saito, K., Ikeda, Y., Nambu, Y., and Yashima, M., High Proton Conduction in the Octahedral Layers of Fully Hydrated Hexagonal Perovskite-Related Oxides, *J. Amer. Chem. Soc.,* 2024, vol. 146, p. 18544.
24. Andreev, R., Korona, D., Anokhina, I., and Animitsa, I., Proton and oxygen-ion conductivities of hexagonal perovskite $Ba_5In_2Al_2ZrO_{13}$, *Materials*, 2022, vol. 15, no. 11, p. 3944.
25. Andreev, R.D., Anokhina, I.A., Korona, D.V., Gilev, A.R., and Animitsa, I.E., Transport properties

of In^{3+}- and Y^{3+}-doped hexagonal perovskite $Ba_5In_2Al_2ZrO_{13}$, *Russ. J. Electrochem.*, 2023, vol. 59, p. 190.

26. Andreev, R.D., and Animitsa, I.E., Protonic transport in the novel complex oxide $Ba_5Y_{0.5}In_{1.5}Al_2ZrO_{13}$, *Ionics,* 2023, vol. 29, no. 11, p. 4647.
27. Andreev, R.D., Korona, D.V., Vlasov, M.I., and Animitsa, I.E., Protonic ceramics $Ba_5In_{2-x}Y_xAl_2ZrO_{13}$ with the perovskite-related hexagonal structure for solid oxide fuel cells: synthesis, optical band gap and transport properties, *Ceramics International*, 2024. https://doi.org/10.1016/j.ceramint.2024.04.227
28. Andreev, R., and Animitsa I., Transport properties of intergrowth structures $Ba_5In_2Al_2ZrO_{13}$ and $Ba_7In_6Al_2O_{19}$, *Appl. Sci.*, 2023, vol. 13, no. 6, p. 3978.
29. Shannon, R., Revised effective ionic radii and systematic studies of interatomic distances in halides and chalcogenides, *Acta Crystallogr. Sect. A Cryst. Phys. Diffr. Theor. Gen. Crystallogr.*, 1976, vol. 32, p. 751.
30. Tarasova, N., and Animitsa, I., Materials $A^{II}LnInO_4$ with Ruddlesden–Popper structure for electrochemical applications: relationship between ion (oxygen-ion, proton) conductivity, water uptake, and structural changes, *Materials*, 2022, vol. 15, no. 1, p. 114.
31. Chebotin, V.N., and Perfilev, M.V., *Electrochemistry of solid electrolytes* (in Russian), Moscow: Khimiya, 1978. 313 p.
32. Sammells, A.F., Kendall, K.R., Navas, C., Thomas, J.K., Loye, H.C., Amsif, M., and Hayashi, H., Structural consideration on the ionic conductivity of perovskite-type oxides, *Solid State Ionics*, 1999, vol. 122, p. 1.